(특별강연I)

PREDICTION OF AIR QUALITY OVER THE SEOUL METROPOLITAN AREA

In Young Lee*
Environmental Research Division, Argonne National Laboratory
Argonne, IL 60439 U.S.A.

Il Soo Park and Ki Duck Choi
Atmospheric Research Division, National Institute of Environmental Research
613-2 Bulkwang-dong, Eunpyung-ku, Seoul 122-040 Korea

Abstract

Numerical studies have been made to examine the air quality over the Seoul metropolitan area considering the effects of mesoscale meteorology and chemically reactive trace gases emitted into the atmosphere on evolution of chemical species concentrations, chemical composition and size distribution of airborne particles, and optical properties of aerosols. For this purpose, a three-dimensional, time-dependent flow model has been coupled with modules for radiative transfer, air chemistry, and aerosol physics. The changes in size distribution and chemical composition of aerosols are calculated considering heterogeneous nucleation, heteromolecular diffusion, and coagulation. The effect of radiative cooling, complex terrain, and variable land-use on mesoscale flow characteristics have been examined and the pollution evolution has been evaluated in terms of chemical transformation, transport and diffusion of chemical species, and aerosol evolution. Simulations indicate that the strength and structure of the wind are controlled mainly by terrain features, ambient wind conditions, and effective radiative cooling rates. On the other hand, the transport and transformation of chemical species are largely controlled by various physical and chemical processes, while the visibility field responds closely to the field of effective aerosol concentrations.

1. Introduction

Anthropogenic emissions of chemical species and dust particles have significantly increased their atmospheric concentrations and reduced visibility due to the changes in physicochemical properties of aerosols (Crutzen, 1987). Reactions of nitrogen oxide and sulfur dioxide emitted from fossil fuel combustion can produce embryos of sulfate and nitrate, which modify the size distributions and the chemical compositions of particles. Such properties determine the effect of aerosols on solar and infrared radiation balance in the atmosphere and the ability of aerosols to serve as cloud condensation nuclei. The effect of air pollution depend to a considerable degree on secondary reaction products. The formation of such products is controlled by the relative composition of pollutants and atmospheric conditions. The air quality in Seoul

---

* Currently with the National Institute of Environmental Research, Ministry of Environment, Korea.

may be diagnosed as a combination of two types: London smog (conversion of sulfur dioxide to sulfate) and Los Angeles smog (production of ozone and other oxidants by nitrogen oxides and various hydrocarbons). It is now well established that considerable quantities of ozone are produced photochemically in Seoul, where concentrations of greater than 100 ppb are often found. On the other hand, the sulfate content in aerosol over the Seoul metropolitan area is not well known. The increase of effective aerosol concentrations coupled with high relative humidity can severely reduce visibility. The clean air policy of the Ministry of Environment, Korea, is designed to reduce the amount of deposition of acidifying pollutants. The strategy is a significant reduction of SO_2 emissions. However, lessening of acid deposition is not the only important benefit of the emission control strategy. The increase of NO_x emissions will contribute much to the visibility reduction associated with regional haze. Although one can get a qualitative sense of how visibility might improve by examining historical regional scale trends in regional emission totals and regional visibility (Trijonis *et al.*, 1990), quantification of the expected improvement requires model simulations. The critical supersaturation to activate typical urban aerosols is quite low, because large amounts of hygroscopic compounds such as sulfates are present. Some experimental analysis relating the patterns between local air circulation and chemical species concentrations over the Colorado mountain area have improved our understanding of the mechanisms by which winds and concentration patterns evolve (Lee *et al.*, 1995).

Figure 1 presents the topographic features of the target area. Seoul metropolitan area is surrounded by mountains except to the west. Jung-ku (the central administrative district of Seoul) is located at x=37 km and y=35 km on the map scale (hereafter as x,y = 37,35). In the north, the Bukhansan is located at x,y = 38,47 with the ridge extending to Dobongsan at x,y = 40,52 and Sulaksan is located at x,y = 47,52, about 7 km east of Dobongsan. In the south, Seoul is surrounded by many mountains including the Kwanaksan in the middle (x,y = 36,24) and Chungryangsan in the far east of the target area (x,y = 57,26). In the east, Seoul is surrounded by the Chunmasan range. Seoul is open to west and northwest with the Kimpo international airport at x,y = 20,36, about 17 km west of the central district of Seoul. The Hangang enters the target area from the east at y = 39 km, runs southwest to reach x,y = 37,32, and then the course changes to northwest arriving at the northwestern corner of the target area. The Hangang divides the target area into Kangbuk and Kangnam districts.

The complex terrain will modify the prevailing wind properties by channeling through valleys, blocking by mountains, and forming wake regions in the lee side of the mountains. The target area may be divided into a few distinguishable land-use categories such as city, forest, farmland, and water. For a comprehensive examination of the effects of air pollution on the life-cycle of chemical species and optical properties of aerosols, many processes associated with air circulation and air chemistry are needed. In this respect, a comprehensive model has been developed to understand transport, dispersion, and transformation of chemical species, and to examine the physicochemical properties of aerosols. The model computes the evolution of momentum, thermal and moisture variables, chemical species, and particulate concentration. The physicochemical process includes homogeneous gas kinetics, heterogeneous nucleation, heteromolecular diffusion, and coagulation. Sensitivity studies have been carried out to examine the aerosol evolution under variable atmospheric conditions and to estimate the anthropogenic effect of aerosols on optical properties. The transport and dispersion characteristics are evaluated in terms of

ambient meteorological conditions, source strength of air pollutants, physicochemical processes, and geographical features.

2. Basic Conservation Equations

The equations for momentum and the continuity are written as

$$\frac{\partial}{\partial t}(\rho V) + \nabla \bullet \rho VV = -\nabla p + \nabla \bullet (\mu_m \nabla V) + S_m + \rho g k \bullet B, \text{ and} \tag{2.1}$$

$$\frac{\partial \rho}{\partial t} + \nabla \bullet \rho V = 0, \tag{2.2}$$

where

$$V \equiv (u, v, w),$$

$$\nabla \bullet \equiv \left(\frac{\partial}{\partial x}, \frac{\partial}{\partial y}, \frac{\partial}{\partial z}\right),$$

$$S_m \equiv \left(\nabla \bullet \mu_m \frac{\partial}{\partial x} V, \nabla \bullet \mu_m \frac{\partial}{\partial y} V, \nabla \bullet \mu_m \frac{\partial}{\partial z} V\right),$$

ρ is the density of air, μ_m is the viscosity of air, and p is the dynamic air pressure. In the last term of (2.1), B represents the net buoyancy due to the virtual temperature differences minus the drag of liquid water.

The conservation equations for air temperature, water vapor mixing ratio, species concentrations, and aerosol number density are written as

$$\frac{\partial}{\partial t}(\rho T) + \nabla \bullet (\rho VT) = \nabla \bullet (K \nabla T) + \frac{L_v}{c_p}\left(\frac{\delta(\rho q)}{\delta t}\right)_{COND} + \frac{\rho T}{c_p} Q, \tag{2.3}$$

$$\frac{\partial}{\partial t}(\rho q) + \nabla \bullet (\rho Vq) = \nabla \bullet (K \nabla q) + \left(\frac{\delta(\rho q)}{\delta t}\right)_{COND}, \tag{2.4}$$

$$\frac{\partial}{\partial t}(\rho C_i) + \nabla \bullet (\rho VC_i) = \nabla \bullet (K \nabla C_i) + \left(\frac{\partial(\rho C_i)}{\partial t}\right)_{CHEM} - \left(\frac{\partial(\rho C_i)}{\partial t}\right)_{NUCL}, \text{ and} \tag{2.5}$$

$$\frac{\partial}{\partial t}(\rho n_j) + \nabla \bullet (\rho V n_j) =$$

$$\nabla \bullet (K \nabla n_j) + \left(\frac{\partial(\rho n_j)}{\partial t}\right)_{NUCL} + \left(\frac{\partial(\rho n_j)}{\partial t}\right)_{COAG} - \left(\frac{\partial(\rho n_j)}{\partial t}\right)_{DIFF} . \quad (2.6)$$

where T, q, C_i, and n_j denote the air temperature, water vapor mixing ratio, species concentration [i = 1, 2, ..., 26: 26 chemical species], and aerosol number density [j = 1, 2, ..., 20: 20 size categories], respectively, L_v is the latent heat of vaporization, c_p is the specific heat of air, and K is the diffusivity of air. In the last term of (2.3), Q denotes the heating rate per unit mass of air. In (2.3) and (2.4), the term $[\partial(\rho q)/\partial t]_{COND}$ represents the changes in water vapor mixing ratio due to nonadiabatic processes. In a cloud-free environment, $[\partial(\rho q)/\partial t]_{COND} = 0$. In (2.5), the terms $[\partial(\rho C)/\partial t]_{CHEM}$ and $[\partial(\rho C)/\partial t]_{NUCL}$ represent the concentration changes due to homogeneous chemical reactions and heterogeneous nucleation, respectively. In (2.6), $[\partial(\rho n)/\partial t]_{NUCL}$, $[\partial(\rho n)/\partial t]_{COAG}$, and $[\partial(\rho n)/\partial t]_{DIFF}$ represent the changes of the aerosol number density due to heterogeneous nucleation, coagulation, and heteromolecular diffusion. At present, the values for eddy viscosity are determined diagnostically by following the approaches of Sommeria (1976).

The radiative forcing is calculated following the approach of Oh (1989). The spectrum of solar radiation is divided into three contributions: Rayleigh scattering, ozone absorption, and water vapor absorption. The spectrum of long-wave radiation is divided into four bands depending on absorbers: water vapor band centers, water vapor band wings, CO_2 band, and O_3 band. A two-stream, delta-Eddington method, economical and suitable for simulations of atmospheric processes under variable atmospheric conditions, is employed for calculations of solar radiation fluxes. The downward and upward fluxes of long-wave radiation are expressed in terms of blackbody radiation and fractions of spectral bands. The fractions for spectral subdivisions are parameterized as a function of temperature and the transmission functions corresponding to spectral bands are calculated using parameterizations. At the surface, the changes in surface temperature by radiative cooling is determined from a prediction equation (Arakawa, 1972) and the sensible and latent heat fluxes at the surface are calculated using bulk aerodynamic methods.

3. Physicochemical Processes

Atmospheric chemical species like nitrogen oxides, sulfur oxides, and reactive hydrocarbons are transformed by a number of physical and chemical pathways. Many chemical reaction schemes have been proposed (Rodhe *et al.*, 1981; Lee, 1983; Chang *et al.*, 1989). The key process affecting tropospheric photochemistry is the photolysis of ozone produced as a result of chemical reactions involving organic pollutants, NO_x (NO and NO_2), and sunlight. The major pathways for O_3 production and destruction are depicted in Fig. 2. When NO and NO_2 are present in sunlight, O_3 formation is initiated by photolysis of NO_2 and significantly increased when hydrocarbons, aldehydes, and other reactive gases are converted to peroxy radicals, which change the

equilibrium by oxidizing NO to NO_2 and cause the ratio NO_2/NO to increase without consuming O_3.

In the Northern Hemisphere, where industrial activities are concentrated, the reaction with CO is a dominant pathway for the OH sink. The HO_2 radical is removed by reaction with O_3 or by HO_2–HO_2 recombination. Then H_2O_2 can be photolyzed, react with the OH radical, or be removed heterogeneously. H_2O_2 plays a significant role in sulfate production through aqueous-phase oxidation of SO_2. The reaction of NO_2 with OH constitutes the dominant sink for odd hydrogen, while the reaction of SO_2 with OH conserves the odd hydrogen. OH and HO_2 account for at least 90% of the predicted SO_2 oxidation rates. During nighttime hours, when the concentration of OH is low, sulfate production decreases rapidly. The NO_x chemistry proceeds even during nighttime hours. The main feature of nighttime NO_x chemistry is the production of NO_3 radical, which is followed by rapid equilibration with N_2O_5. For this study, the Argonne's aerosol model (Lee, 1983) was modified to add gas-phase reactions found to be important (Chang *et al.*, 1989; Carmichael *et al.*, 1986; NAPAP Report, 1991) and to refine the treatment of gas-to-particle conversion.

4. Computational Procedures

A staggered grid system is employed for vector (u, v, and w) and scalar (T, q, C, n, p, and ρ) quantities. The scalar quantities are defined at the centers of the grid cells, while the wind vectors are defined at the midpoints of cell boundaries. Both the vector and scalar quantities are defined at the boundaries as well. We assume that the upwind ambient horizontal velocities at inflow boundaries u and v are held constant, that the forced-flow boundary condition is applied at the outflow region, that shear-free flow is assumed at the top of the model, and that nonslip boundary conditions are applied to all solid surfaces. The set of governing equations is solved on the staggered grid by a finite-volume method. Finite-difference equations are derived by integration of the governing equations over an elementary control area or cell surrounding a grid node. The solution algorithm used for the momentum equation is the semi-implicit method for pressure-linked equations outlined in Patankar (1980). The momentum and pressure fields are determined through iterative adjustment. The discretized momentum equations are solved initially with a pressure field obtained from the previous step; then the pressure field is recalculated from a pressure Poisson equation to yield the pressure change needed to adjust the velocity field to ensure mass continuity. Iteration continues until required adjustments in the momentum and pressure fields are sufficiently small. After the velocity field is obtained, solution fields for air temperature, water vapor mixing ratio, pollutant concentration, and aerosol number density are calculated from conservation equations for T, q, C, and n discretized by a finite-volume method and solved by the successive overrelaxation method.

The disadvantage of incorporating the kinetics model with an aerosol model is the computational cost of integrating the chemical reaction parts of conservation equations. Since the rate equations describing photochemistry involve time constants that are a very small fraction of a second, ordinarily only implicit techniques are used for their solution. However, these techniques require the solution of a large set of linearized equations and impose substantial computational cost. Our chemistry module has been modified to increase efficiency without significant loss of accuracy (Swan and Lee, 1980). First, a partitioning procedure takes advantage of the fact that some

species do not involve time constants that are short compared to the desired integration time step, and thus their concentration equations can be integrated explicitly. The second modification to increase computational efficiency employs computer-generated subroutine codes to solve the equations. These optimal codes do not use loop coding and avoid all operations on zeros. Thus, only nonzero elements of the Jacobian of the implicit partition are calculated, and only nonzero operations are performed to solve the linear set of equations. Because of the extreme sparseness of the array of coefficients defining the linear equation set, the avoidance of computer operations on the zero terms leads to sizable reduction in overall computational cost.

The rate of change in the size of a particle depends on pressure gradients that are due to the differences between the partial pressures of acids in the environment and those at the particle surface, the partitioning ratios of acid molecules, the Knudsen number, particle size, diffusivity, and temperature. If the partial pressure of sulfuric acid in the environment is greater than that at the surface of the particle, the droplet will grow by diffusion, and vice versa. At the same time, the droplet will absorb water molecules to reach equilibrium. The smallest sulfuric acid particles are composed of two molecules of H_2SO_4 and a few molecules of H_2O. The number of H_2O molecules in the smallest droplet is determined by increasing the number until the droplet reaches an equilibrium size with respect to the partial pressure of H_2O in the environment. The changes in size distribution and chemical composition of aerosols are calculated with consideration of heteromolecular diffusion and coagulation processes by using the method proposed by Lee (1983) with some modifications. For this model, we have selected 20 size bins ranging from 0.0004 to 2.4 μm. The aerosol evolution due to coagulation is calculated by following the procedures of Turco *et al.* (1979). The collection kernels depend on the particle size, the diffusivity, and the kinetic velocity of a particle.

The horizontal and vertical grid sizes are set to 2000 and 200 m, respectively. The shear-free level or the model top is set to 3000 m. The emission rates for SO_2, NO_x, CO, total suspended particles (TSP), and total hydrocarbons HC are obtained from literature (Choi *et al.*, 1994). For each chemical species and TSP, the annual emission rates for 2X2 km^2 area are constructed by taking into account of area, line, and point sources. Direct application of the emission inventory to air quality simulations is limited, since the partitioning of the TSP into size categories and the total HC into many types of hydrocarbon such as aldehydes, aromatics, alkanes, alkenes and others is impracticable. The specification of total hydrocarbons is critical for calculations of ozone evolution.

5. Results and Discussion

Numerical experiments have been carried out (1) to examine the physicochemical processes and (2) to predict the mesoscale air quality. For the former case, the chemistry module has been exercised extensively under different atmospheric conditions. On the other hand, the three-dimensional circulation model coupled with modules for processes of radiative transfer, air chemistry, and aerosol physics are used to predict the three-dimensional evolution of dynamic parameters, chemical species mixing ratios, and effective particulate concentrations.

Temporal variations of chemical species, size distribution of the effective particulate, and visibility are interpreted in terms of oxidation rate of sulfur and nitrogen

oxides, relative solar insolation, and relative humidity. First, the general trends associated with the clear-air photochemistry are examined under the constant relative humidity of 85%. We find that both O_3 and NO_2 decreases slowly during the nighttime. O_3 increases rapidly after sunrise reaching a maximum at about 1500 LST, and then decreases moderately thereafter. On the other hand, NO_2 maintains a nearly constant value during daytime and then decreases moderately after sunset. NO reaches a midmorning maximum and decreases slowly thereafter. N_2O_5 decreases sharply at sunrise and increases sharply at sunset because of corresponding NO_3 changes, while HO_2 exhibits rapid changes at sunrise and sunset, opposite those of N_2O_5. As expected, the solar intensity reaches a maximum at noon. The SO_2 concentration decreases slowly during the daytime, mainly because of oxidation processes occurring in association with the free radicals OH and HO_2. The oxidation rate of SO_2 undergoes a diurnal cycle, reaching a maximum of 0.8% h^{-1} at 1300 LST. On the other hand, the NO_2 loss rates show two peaks, immediately after sunrise (18% h^{-1}) and sunset (32% h^{-1}). The behavior of chemical species associated with photolysis agrees closely with our previous analysis (Swan and Lee, 1980).

Figure 3 presents the spectral evolution of aerosol particles. The curves represent the effective suspended particle load (a plot of the mass of aerosol particles in each given size bin) after 9, 12, and 15 hours of real-time simulation with preexisting aerosol particles. We see clearly that the aerosol load increases with time due to physicochemical processes. The embryos produced by heterogeneous nucleation grow by heteromolecular diffusion and coagulation and modify the aerosol properties significantly. Our analysis shows that the total aerosol load can be increased by as much as 40% in 15 hours, and that the scattering area can be increased by about 30%, even though, the diffusional growth of particles is limited under an equilibrium state of the particle-air system. Figure 4 presents the effect of relative humidity on visibility and aerosol density after 9, 12, and 15 hours of real-time simulations. We see that the aerosol density and visibility stay constant until the relative humidity increases to about 70%; that the aerosol number density increases slowly with the increase of relative humidity from 70 to about 85%, and thereafter, increases rapidly; and that the visibility decreases rapidly when the relative humidity becomes greater than about 75%. The aerosol density increases steadily with the increase of simulation time, while the visibility decreases fast with time initially and then, decreases slowly thereafter.

Our analysis shows that the variation of relative humidity and solar insolation affects the evolution characteristics of chemical species and aerosols. NO_2 decreases fast with the increase of relative humidity due mainly to the increased conversion of NO_2 to nitric acid (HNO_3). On the other hand, the rate of conversion from SO_2 to sulfate (SO_4), hydrogen sulfite (HSO_3), hydrogen sulfur pentoxide (HSO_5), and sulfur trioxide (SO_3) proceeds with a moderate rate. The effective suspended particulate (ESP) concentration increases with the increase of relative humidity. However, the rate of increase of ESP proceeds faster than those of visibility reduction, because coagulation and heteromolecular diffusion processes produce larger particles which are not effective either for light scattering or absorption. Ozone evolution shows some interesting features. Daily maximum value of ozone increases with the increase of relative humidity due mainly to the fact that the NO_2/NO ratio increases with the increase of relative humidity, even though the NO_2 concentration decreases with the increase of relative humidity. It is interesting to see that the daily ozone maximum occurs early in the afternoon when the relative humidity is low, and vice versa. It is

also noticed that the daily ozone maximum occurs in the early afternoon during the winter season, while the occurrence is delayed by about one to two hours during the summer time. Ozone, SO_2 and ESP production is higher during the summer season with longer solar hours.

For three-dimensional analysis, the modules for air chemistry and aerosol physics are coupled with the dynamic flow model. Simulations have been carried out for fifteen hours of real time to obtain fields for momentum, chemical species concentration, and ESP, and the visibility field is determined diagnostically. Conventional time splitting is employed to integrate different processes. Time step for momentum fields, moisture and thermodynamic variables, and cloud formation/dissipation processes is set to 100 s. On the other hand, the time steps for calculations of homogeneous gas kinetics, aerosol evolution (heteromolecular diffusion and coagulation), and radiative transfer processes are set to 300 s, 100 s, and 1200 s, respectively. A breezy northwesterly prevailed throughout the simulation period and the air in the lower troposphere was quite dry (the relative humidity never exceeded 50%). In this case, the growth by heteromolecular diffusion associated mainly with the H_2O and H_2SO_4 flux toward particles can be limited. Furthermore, as described in the previous section, the use of the emission rates for TSP and HC is questionable, because the partitioning of the TSP into size categories and the total HC into many types of hydrocarbons is impracticable. TSP categorization and HC specification are critical for calculations of gas kinetics and aerosol evolution.

More than 90% of the source strength can be realized within about 600 m above sea level and the concentration, in general, decreases rapidly with height, though the model top extends vertically to 3000 m. Winds increase with height. The maximum winds at 100-m and 300-m levels are 3.2 and 5.1 m s^{-1}, respectively. Figure 5 presents the 100-m level winds. Here, we see clearly that the local circulation generated by topographic features dominates near the surface, while the winds aloft approach to the prevailing northwesterly. The local winds are mainly controlled by the strength of the wakes generated in the lee side of the mountain ranges and by topographic features. Vortices of various sizes are formed in the lee side of the mountains, while they are channeled, deflected, drained, and blocked. Our analysis show that both the updraft and downdraft regions and their strengths increase with height, and that the downdraft is stronger by about factor of two, indicating that the air traveling across the mountain ranges is lifted first for a short distance and then downdrafted with much faster rate creating clockwise vortices throughout the lee side regions. In Figure 5, we see clearly that the stagnation occurs over areas east of Bukhansan range and south and east of Sulaksan due to the pressure drop in the lee side of mountains, and that the channeled winds are developed along the valley between Kwanaksan and Chungryangsan.

In general, the concentration level decreases steadily with height. The 300-m values, for example, are smaller by about 30% for SO_2 and ESP, and by about 40% for NO_x, while the visibility at 300-m level is greater than that at 100-m level by about 30%. The 100-m fields represent the ground level concentrations closely reflecting the source strength. The plumes, in general, extend southeast covering most of the Seoul metropolitan area. In Seoul, the concentration levels range from 18 to 106 ppb for SO_2, from 86 to 286 ppb for NO_x, and from 22 to 92 $\mu g\ m^{-3}$ for ESP. Our analysis shows that the concentration levels for SO_2 and NO_2 exceeds the yearly standards set by the Ministry of Environment, Korea. Presently, the yearly standards are set to 30 ppb for SO_2 and 50 ppb for NO_x, while the hourly standards are set to 250 ppb for SO_2

and 150 ppb for NO_x. We find that the SO_2 concentration levels are lower than the hourly standards. However, we also find that a large portion of the Seoul metropolitan area is infected by high levels of NO_x concentration, which exceeds the hourly standards (150 ppb). The impact areas cover more than about 24% of the Seoul metropolitan area.

The distribution of ESP concentration depend on the nature of the preexisting aerosol particles, and aerosol evolution preceding particulate emissions and production of nitrate and sulfate embryos. In this study, the initial aerosol distributions are assumed to have distributions similar to the Junge-type continental-background-aerosol and the initial aerosol content is set to 15 $\mu g\ m^{-3}$. We find that the concentration levels reflect the source strength closely, and that the aerosol properties are modified by physicochemical processes considered. The high level areas are located over the Buchun-si and Sucho-ku due mainly to the high particulate emissions. The average ESP concentration, in general, decreases fast with altitude and the dust plume extends southeast covering most of the target area. As shown in Figures 6, the visibility field reflects the ESP and NO_x fields closely. The impact areas with the visibility less than 10 km cover about 24% as in the NO_x case, indicating clearly that the visibility impairment is due to the combined effect of high ESP and high NO_2 concentrations. The average visibility increases rapidly with height.

The 100-m level ozone contours at 1500 LST are shown in Figure 7. Initially, the background ozone was set to 22 ppb. As described in the previous section, the ozone level increases steadily after the sunrise, reaches a maximum early in the afternoon, and then starts to decrease thereafter. The three-dimensional case reveals that the increase of the ozone level is augmented significantly due to the local emissions of NO_x and HC. In this case, the computed maximum was 74 ppb at 1340 LST over the central district . At this time, the ozone level over this district exceeded 8-hour standard (the 8-hour standard for ozone is set to 60 ppb). In general, we find that the ozone level increases with time reaching a maximum in the early afternoon. The maxima over the target area are 54 ppb at 0900 LST, 68 ppb at 1200 LST, and 62 ppb at 1500 LST. Since the ozone level depends much on photolysis rate, local traffic and atmospheric conditions such as cloud cover should be considered in the model for better prediction.

6. Conclusions and Future Studies

Results produced from a sulfate aerosol model involving of photochemical reactions and particle growth by diffusion and coagulation show that the SO_2 and NO_2 transformation rates undergo a diurnal cycle with a maximum of 0.8% h^{-1} and 32% h^{-1}, respectively; and that the polluted air can modify the physicochemical properties of aerosols by adding as much as 40% of sulfate to existing aerosols and increase the scattering area by about 30%. The visibility reduction is controlled by ESP and NO_2 concentrations to form a large portion of the Seoul metropolitan area with visibility less than 10 km. It is premature to perform an indepth analysis at this stage of research. However, some preliminary results have been produced from a three-dimensional, time-dependent air quality model. We find that the momentum properties can be simulated and interpreted in terms of flow conditions and topographical configurations. The strength of the local circulation in Seoul and its distribution are controlled mainly by the ambient wind conditions, effective radiative cooling rates, and topographic

features. Simulated contaminants and visibility reduction are controlled mainly by physicochemical processes including homogeneous gas kinetics, heterogeneous nucleation, hetromolecular diffusion, and coagulation, and by local circulation formed in the lower portion of the atmosphere, dispersion, and ambient winds. The transport of pollutants from the lower to the upper portion of the target area is largely controlled by diffusional processes.

More numerical studies are planned with an improved model. Addition of a cloud module (Lee and Park, 1994) will allow examination of flow properties under cloudy conditions. The chemistry module will be modified as needed and extensive numerical experiments will be made until reasonable concentration patterns for secondary chemical species such as ozone can be obtained. Systematic and differential method will be introduced to partition properly the source inventory of TSP and HC.

Acknowledgments

Thanks are due to Dr. M.L.Wesely at Argonne National Laboratory and Dr. T.Y. Lee at Yonsei University, Seoul for useful discussions. This work was supported by the National Institute of Environmental Research, Ministry of Environment, Korea.

References

Arakawa, A.: 1972, 'Design of the UCLA General Circulation Model', Technical Report No. 7, Department of Meteorology, University of California, Los Angeles.

Carmichael, G.R., L.K. Peters, and T. Kitata: 1986, 'A second generation model for regional-scale transport/chemistry/deposition', *Atmos. Environ.*, **20**, 173-188.

Chang, Y.S., G.R. Carmichael, H. Kurita, and H. Ueda: 1989, 'The transport and formation of sulfates and nitrates in central Japan', *Atmos. Environ.*, **23**, 1749-1773.

Choi, D.I., H.J. Lee, J.S. Han, D.J. Hwang, B.G. Kim, S.G. Chang, G.R. Cho, G.C. Kim, Y.D. Hong, B.H. Kim, S.Y. Choi, P.S. Kwon, J.S. Park, E.J. Han, C.K. Shin, S.D. You, S.D. Kim, T.S. Kim, S.Y. Cho, and J.I. Sim: 1994, 'A study on visibility and smog phemena in Seoul metropolitan area (I) Sources of visibility Impairing materials and mechanisms', Report NIER No. 94-05-420, National Institute of Environmental Research.

Crutzen, P.A.: 1987, 'Acid rain at the K/T boundary', *Nature*, **330**, 108-109.

Lee, I.Y.: 1983, 'Formation of sulfates in a cloud-free environment', *J. Climate Appl. Meteor.*, **22**, 163-170.

Lee, I.Y., R.L. Coulter, H.M. Park, J.-H. Oh: 1995, 'Numerical simulation of nocturnal drainage flow properties in a rugged canyon', *Boundary-Layer Meteorol.*, **72**, 305-321.

Lee, I. Y. and Park, H. M.:1994, 'Comparison of Microphysics Parameterizations in a Three-Dimensional Dynamic Cloud Model', *Atmos. Environ.*, **28**, 1615-1625.

NAPAP Report: 1991, 'The regional acid deposition model and engineering model', in NAPAP State of Science & Technology, Vol. I, Report 4. P.M. Irving, ed., The U.S. National Acid Precipitation Assessment Program.

Oh, J.-H.: 1989, 'Physically-Based General Circulation Model Parameterization of Clouds and Their Radiative Interaction', Ph.D. Dissertation, Oregon State University, Corvallis, Oregon.

Patankar, S. V.: 1980, *Numerical Heat Transfer and Fluid Flow*, McGraw-Hill, New York.

Rodhe, H., P. Crutzen, and A. Vanderpol: 1981, 'Formation of sulfuric and nitric acid in the atmosphere during long-range transport', *Tellus*, **33**, 132-141.

Sommeria, G.: 1976, 'Three-Dimensional Simulation of Turbulent Processes in an Undisturbed Trade Wind Boundary Layer', *J. Atmos. Sci.*, **33**, 216–241.

Swan, P.R., and I.Y. Lee: 1980, 'Meteorological and air pollution modeling for an urban airport', *J. Appl. Meteor.*, **19**, 534-544.

Trijonis, J.D., W.C. Malm, M. Pitchford, W.H. White, R. Charlson and R. Husar, 1990: *Visibility: Existing and Historical Conditions - Causes and Effects.* NAPAP Repost 24, National Acid Deposition Assessment Program, Washington, DC.

Turco, R.P., P. Hamill, O.B. Toon, R.C. Whitten, and C.S. Kiang: 1979, 'The NASA-Ames Research Center stratospheric aerosol model', NASA Tech. Pap. 1362, National Aeronautics and Space Administration, Washington, D.C.

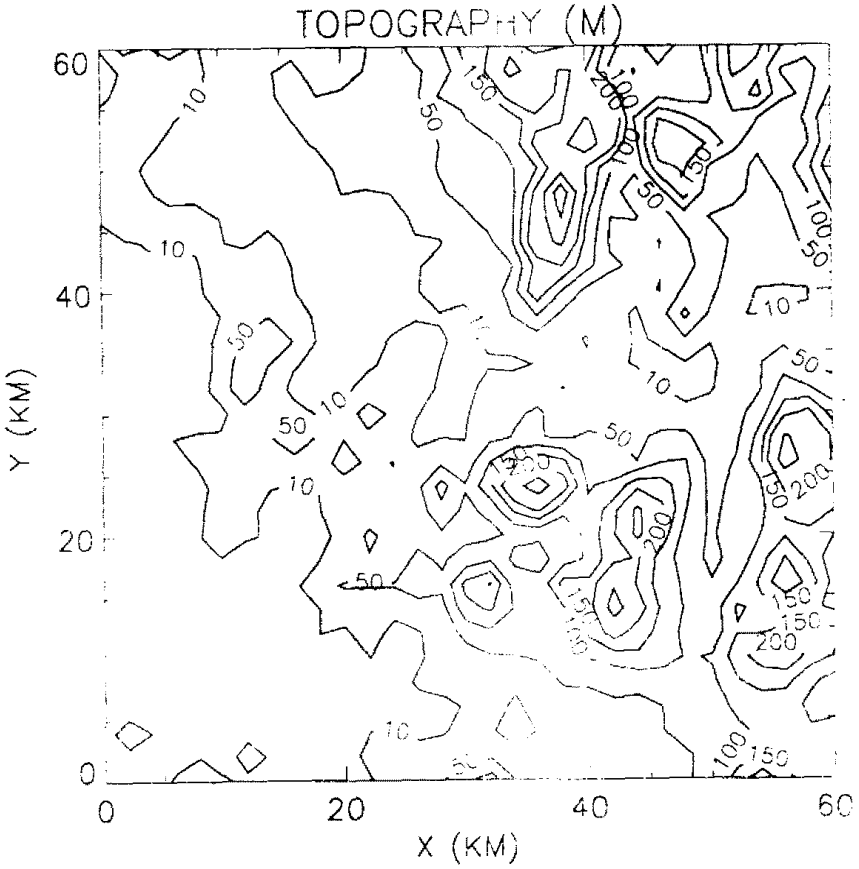

Figure 1. Target area for comprehensive air quality modeling. The topography is expressed in meters.

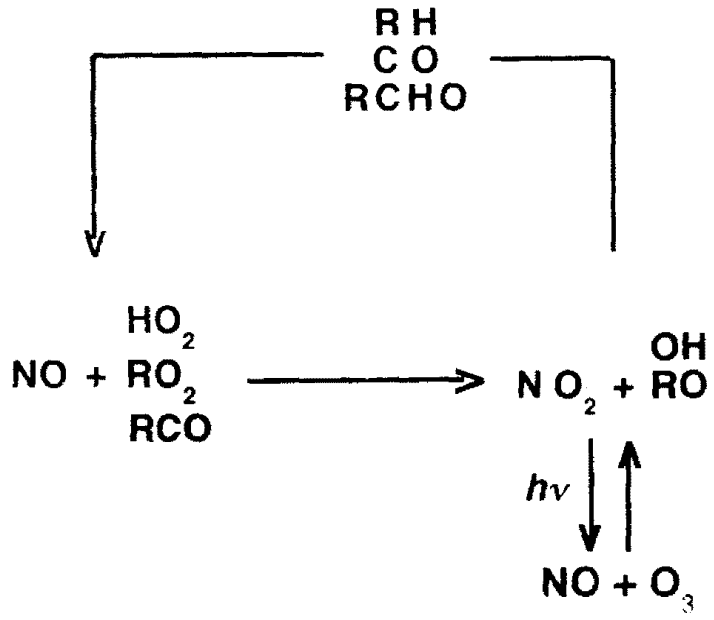

Figure 2. Schematic diagram of chemical pathways for ozone production.

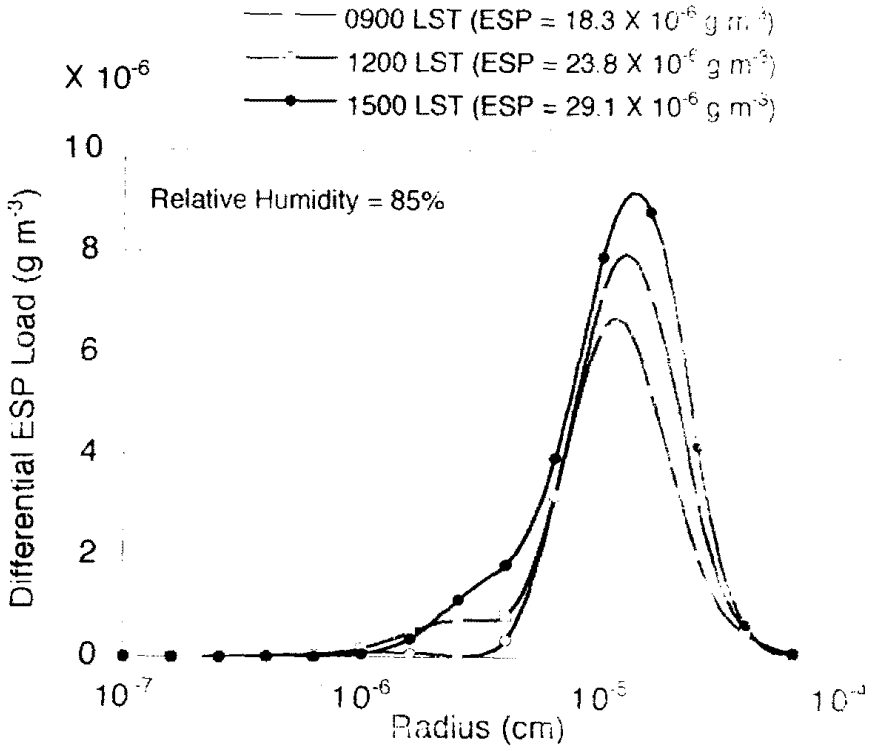

Figure 3. Loading of effective suspended particulate after 9, 12, and 15 hours of real-time simulation.

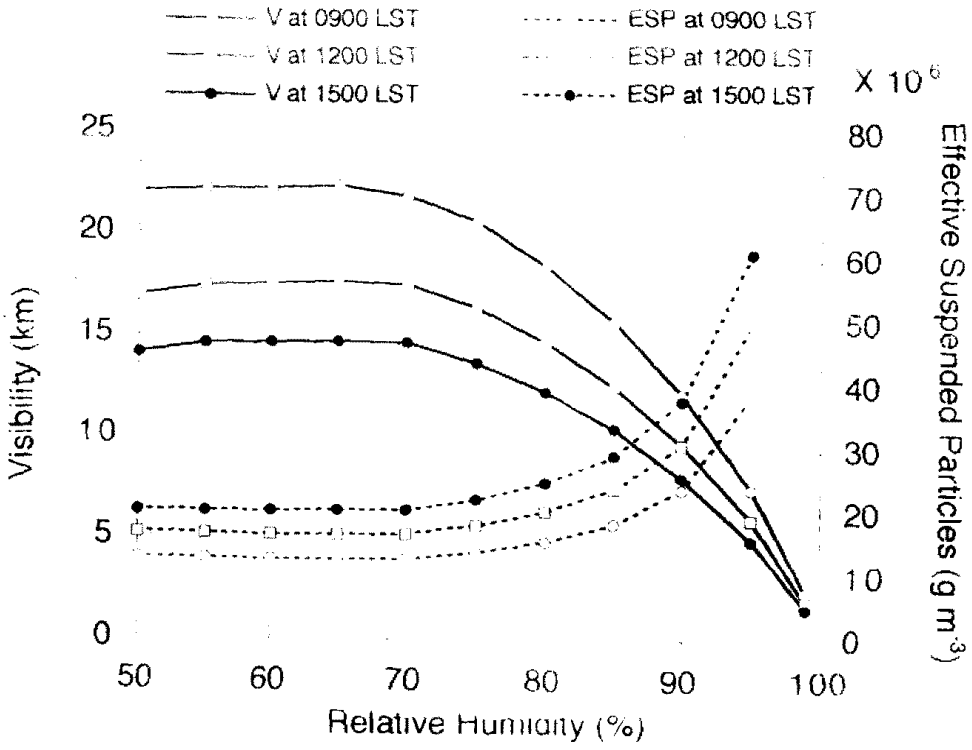

Figure 4. Effect of relative humidity on visibility and effective suspended particulate.

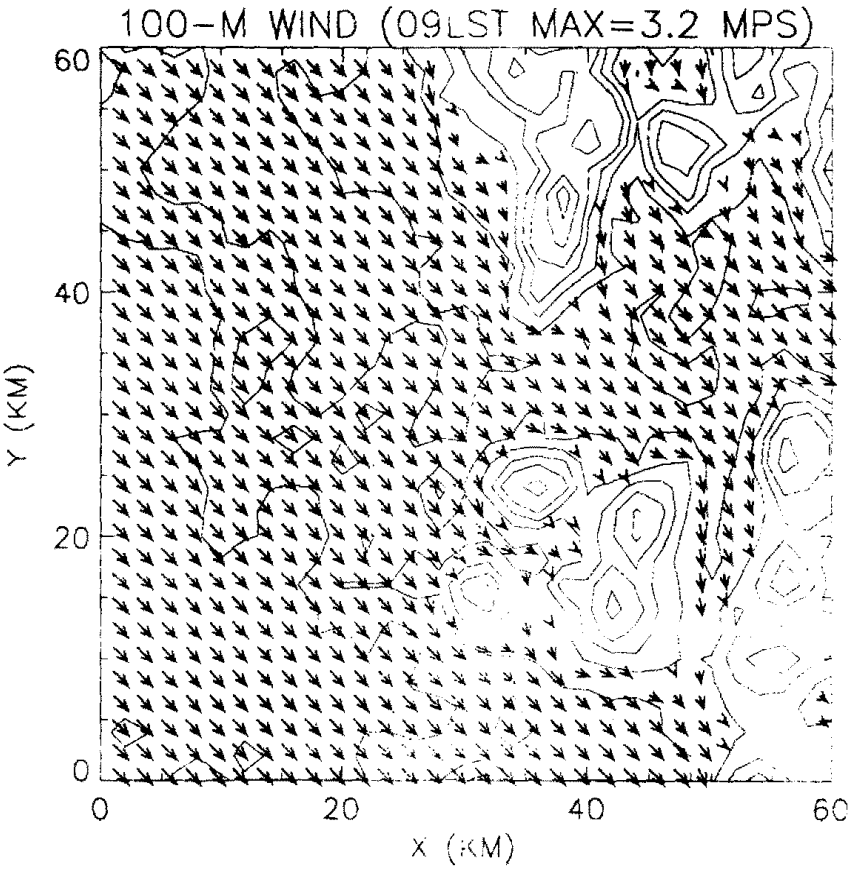

Figure 5. Momentum fields at 0900 LST at 100-m level. The maximum winds at 100-m is 3.2 m s^{-1}.

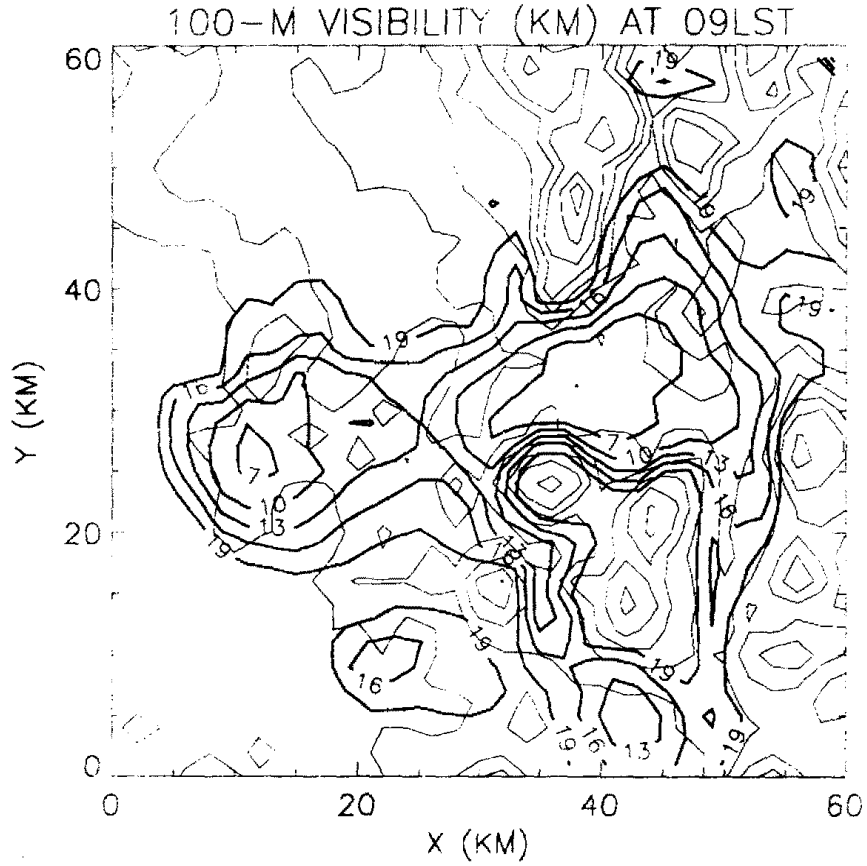

Figure 6. 100-m level visibility field (km) at 0900 LST.

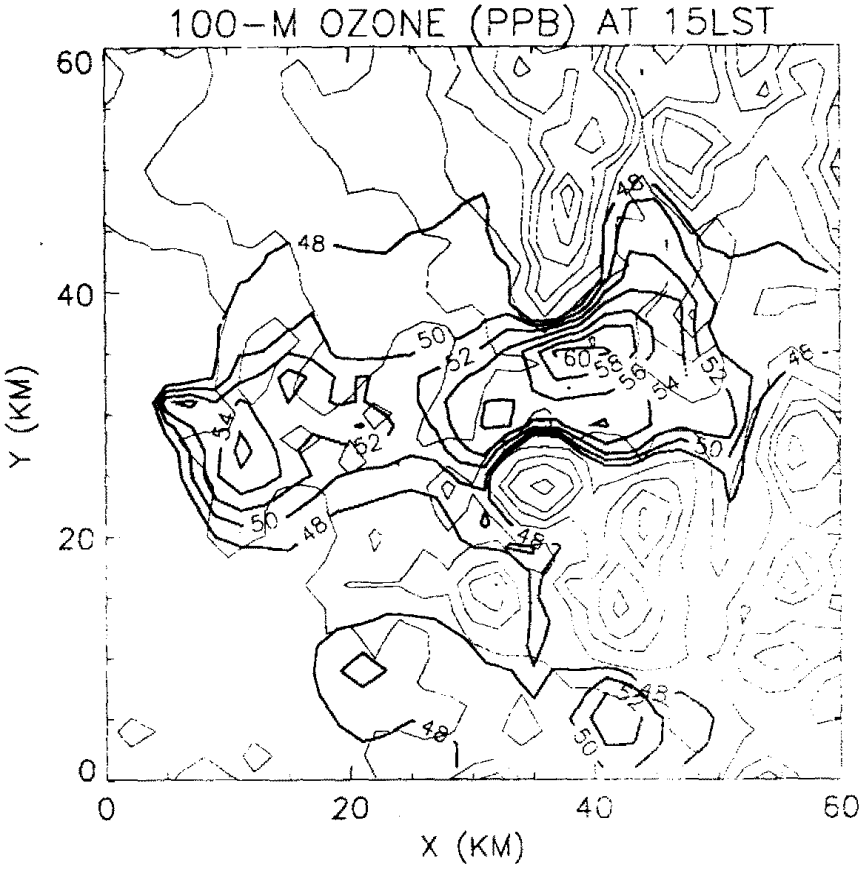

Figure 7. 100-m level ozone concentration contours (ppb) at 1500 LST.